university of groningen

University Medical Center Groningen

University of Groningen

Concentric Tube-Inspired Magnetic Reconfiguration of Variable Stiffness Catheters for Needle Guidance

Richter, Michiel; Venkiteswaran, Venkatasubramanian Kalpathy; Misra, Sarthak

Published in:
IEEE Robotics and Automation Letters

DOI:
10.1109/LRA.2023.3307294

IMPORTANT NOTE: You are advised to consult the publisher's version (publisher's PDF) if you wish to cite from it. Please check the document version below.

Document Version
Publisher's PDF, also known as Version of record

Publication date:
2023

Link to publication in University of Groningen/UMCG research database

Citation for published version (APA):
Richter, M., Venkiteswaran, V. K., & Misra, S. (2023). Concentric Tube-Inspired Magnetic Reconfiguration of Variable Stiffness Catheters for Needle Guidance. *IEEE Robotics and Automation Letters*, *8*(10), 6555-6562. https://doi.org/10.1109/LRA.2023.3307294

Copyright
Other than for strictly personal use, it is not permitted to download or to forward/distribute the text or part of it without the consent of the author(s) and/or copyright holder(s), unless the work is under an open content license (like Creative Commons).

The publication may also be distributed here under the terms of Article 25fa of the Dutch Copyright Act, indicated by the “Taverne” license. More information can be found on the University of Groningen website: https://www.rug.nl/library/open-access/self-archiving-pure/taverne-amendment.

Take-down policy
If you believe that this document breaches copyright please contact us providing details, and we will remove access to the work immediately and investigate your claim.

Downloaded from the University of Groningen/UMCG research database (Pure): http://www.rug.nl/research/portal. For technical reasons the number of authors shown on this cover page is limited to 10 maximum.

Concentric Tube-Inspired Magnetic Reconfiguration of Variable Stiffness Catheters for Needle Guidance

Michiel Richter, Venkatasubramanian Kalpathy Venkiteswaran, *Member, IEEE*, and Sarthak Misra, *Senior Member, IEEE*

***Abstract*—Guiding catheters assist in delivering hazardous equipment such as needles through non-solid mediums likecavities and vasculature. Traditionally, metallic needles are passed through metallic guiding catheters, which are limited to linear paths or require anatomy-specific designs. Recently, variable stiffnessactive guiding catheters (AGCs) made of shape memory polymers have been developed. These AGCs can adapt to anatomy and guide equipment in their rubber and glass phases, respectively. However, passing needles can cause deflectionof the AGC and misalignment with the target. To address this, magnetic configuration of AGCs based on concentric-tube models is proposed to compensate for needle-induced AGC deflection. Experiments demonstrate shape configuration of AGCs using magnetic fields computed pre-experimentally, followed by needle guidance to three different targets. The results show AGC deflection of up to 69° and needle-induced backward deflection up to 39°, with a maximum target misalignment of 4°.**

***Index Terms*—Surgical robotics: steerable catheters/needles, mechanism design, medical robots and systems, cosserat rods.**

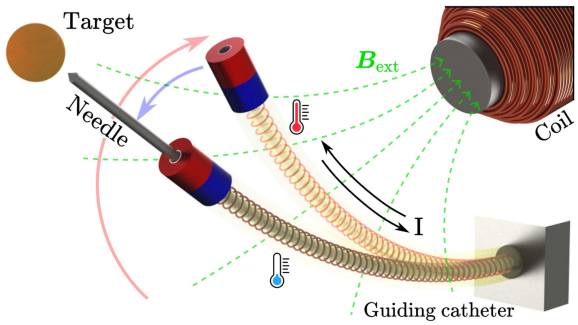

Fig. 1. Concept: An active guiding catheter (AGC) and needle with similar flexur rigidity are arranged concentrically. Initially, the AGC is heated using current (I) to increase flexibility. Then, an external magnetic field ($\boldsymbol{B}_{\text{ext}}$) is used to magnetically deflect the AGC. Next, the AGC is cooled to fix its shape and achieve a new pre-curvature. Finally, the needle is inserted through the AGC, causing the AGC to deform and align with the target.

I. Introduction

GUIDING catheters provide enclosed pathways for access by surgical instruments to target sites [1]. For example, flexible polymer-based catheters guide balloons and stents for endovascular interventions [2]. Also, rigid metallic catheters guide needles along linear paths [3], whereas nested pre-curved metallic catheters can guide needles along curved paths [4], [5]. In the latter case, an anatomy-specific design is required to ensure safe extension in the body [6].

Recently, variable stiffness active guiding catheters (AGCs) have been developed that hold potential for enabling configurable curved needle pathways [7], [8]. Specifically, AGCs made from shape memory polymers exhibit a temperature-dependent shift in elastic modulus around a glass-transition temperature, between the rubber (flexible) and glass (stiff) phase of the polymer [9]. Although the elastic modulus of a shape memory polymer ranges between a few MPa to GPa [8], common needle materials such as nitinol or stainless steel have an elastic modulus on the order of tens to hundreds of GPA [10]. Consequently, AGCs and needles may have a similar bending stiffness and behave as a balanced-stiffness concentric-tube robot (CTR) [6].

Balanced-stiffness CTRs are defined as a collection of nested rods with similar bending stiffnesses, different pre-curvatures, and the ability to rotate and translate relative to each other [11]. These CTRs can be modeled with Cosserat rod theory [12], which accommodates variations in pre-curvature, material properties, cross-sectional geometry, and external loading between rods [13], [14]. Within Cosserat rod theory, the shapes of unloaded and loaded rods are described by pre-curvature and curvature vectors, respectively [15].

An AGC has two states: flexible and stiff, associated with the rubber- and glass-phase of the shape memory polymer, respectively. In the rubber phase, the curvature can be easily changed using external actuation [9]. After transitioning to the stiff state, the curvature can be shape-locked to become the glass-phase AGC pre-curvature. Through modeling, the glass-phase pre-curvature can be configured to compensate for any additional deflection due to a passing needle.

Magnetically-assisted reconfiguration of an AGC removes the need for internal actuation (e.g., tendons), which permits integration of heating and cooling mechanisms [16], [17]. The

Manuscript received 24 April 2023; accepted 12 August 2023. Date of publication 21 August 2023; date of current version 4 September 2023. This letter was recommended for publication by Associate Editor Xiang LI and Editor Clement Gosselin upon evaluation of the reviewers' comments. This work was supported by the European Research Council through the European Union's Horizon 2020 Research and Innovation Programme under Grant 866494 Project – MAESTRO. *(Corresponding author: Michiel Richter.)*

Michiel Richter and Venkatasubramanian Kalpathy Venkiteswaran are with the Surgical Robotics Laboratory, Department of Biomechanical Engineering, University of Twente, 7500 AE Enschede, The Netherlands (e-mail: m.richter@utwente.nl; v.kalpathyvenkiteswaran@utwente.nl).

Sarthak Misra is with the Surgical Robotics Laboratory, Department of Biomechanical Engineering, University of Twente, 7500 AE Enschede, The Netherlands, and also with the Surgical Robotics Laboratory, Department of Biomedical Engineering, University of Groningen and University Medical Centre Groningen, 9713 GZ Groningen, The Netherlands (e-mail: s.misra@utwente.nl).

This letter has supplementary downloadable material available at https://doi.org/10.1109/LRA.2023.3307294, provided by the authors.

Digital Object Identifier 10.1109/LRA.2023.3307294

2377-3766 © 2023 IEEE. Personal use is permitted, but republication/redistribution requires IEEE permission.
See https://www.ieee.org/publications/rights/index.html for more information.

Authorized licensed use limited to: University of Groningen. Downloaded on February 16,2024 at 12:25:47 UTC from IEEE Xplore. Restrictions apply.

addition of a magnetic dipole makes the AGC susceptible to deformation by a magnetic wrench, exerted by an external magnetic field [9]. Magnetic fields are generated by either permanent- or electromagnet-based actuation systems, which are able to manipulate the fields to exert prescribed wrenches on dipoles in their actuation workspace [18].

To the authors' knowledge, the use of AGCs for needle guidance, their modeling as balanced-stiffness concentric-tube robots, and their magnetically-assisted reconfiguration in order to compensate for needle-induced backward deflection, shown in Fig. 1, have not yet been explored. This study applies a concentric-tube model based on Cosserat rod theory for shape configuration of a shape memory polymer-based AGC, using magnetic fields from an electromagnetic actuation systems. Experiments show that the AGC shape can compensate for needle-induced backward deflections and guide the needle to various targets in the actuation workspace.

II. Theory

In this section, a summary of the static modeling theory for Cosserat rods is presented, but comprehensively reported in [15], [19]. This is followed by the application of Cosserat rod theory in modeling concentric-tube robots [20]. Thereafter, computation of curvature vectors of deformed rods is discussed based on arc-parameterization of their centerline curve and Frenet-Serret reference frames.

A. Cosserat Rods

Consider a rod with a known length (l). The rod is characterized by a centerline parameter $(s \in [0, l])$, which defines a set of material states $\{\boldsymbol{p}(s),\ \boldsymbol{q}(s),\ \boldsymbol{n}(s),\ \boldsymbol{m}(s)\}$, where $\boldsymbol{p}(s) \in \mathbb{R}^3$ is the centerline curve, $\boldsymbol{q}(s) \in \mathbb{H}$ an orientation quaternion, $\boldsymbol{n}(s) \in \mathbb{R}^3$ the internal force, and $\boldsymbol{m}(s) \in \mathbb{R}^3$ the internal moment [21]. Arc-derivatives of the material states $(\{\dot{\boldsymbol{p}}(s),\ \dot{\boldsymbol{q}}(s),\ \dot{\boldsymbol{n}}(s),\ \dot{\boldsymbol{m}}(s)\})$ determine their propagation along s, where $\dot{*}(s) = \partial *(s)/\partial s$.

Arc-derivatives of material states are ordinary differential equations (ODEs) that depend on external distributed forces and moments $\{\boldsymbol{f}(s), \boldsymbol{\tau}(s)\}$ to determine the magnitude of rod deformation [21]. The problem of calculating the deformed rod shape can be formulated as a boundary value problem (BVP) [15]. Generally, the solution process involves discretizing the rod centerline (s) into a descrite number of segments $(D \in \mathbb{Z}^+)$ with length $\Delta s := l/D$ [22]. Proximal boundary conditions may include pose, whereas distal boundary conditions include loading. Solving the BVP provides a shape solution,

$$\boldsymbol{Y} = \begin{bmatrix} \boldsymbol{y}(0) & \boldsymbol{y}(\Delta s) & \dots & \boldsymbol{y}(D\Delta s) \end{bmatrix} \in \mathbb{R}^{13\times(D+1)}, \quad (1)$$

including material states at discrete points along the centerline, where $\boldsymbol{y}(s) = \langle \boldsymbol{p}(s), \boldsymbol{q}(s), \boldsymbol{n}(s), \boldsymbol{m}(s) \rangle \in \mathbb{R}^{13}$ and $\langle * \rangle$ represents a vectorization operation to a column vector.

B. Concentric-Tube Robots

Combining nested rods with different pre-curvatures constitutes a concentric-tube robot (CTR). For ease of representation, consider $i \in \{1, 2\}$ rods ($i = 1$ represents the outer rod) and assume that $l_1 \geq l_2$. The objective is to compute the deformed centerline curve of the outer rod (which is the same as all inner rods). That is, compute $\{\boldsymbol{p}_1(s), \boldsymbol{q}_1(s)\}$, as a result of the passing inner rod $(i = 2)$, where $\boldsymbol{q}_i(s) = \langle \mathrm{Re}(q_i), \mathrm{Im}(\boldsymbol{q}_i) \rangle \in \mathbb{H}$ $(\mathrm{Re}(q_i) \in \mathbb{R},\ \mathrm{Im}(\boldsymbol{q}_i) \in \mathbb{R}^3)$ is an orientation quaternion.

Each (cylindrical) rod in a CTR has an elastic modulus (E_i), shear modulus (G_i), second moment of area $(I_i = I_{x,i} = I_{y,i})$, polar moment of area $(J_i = 2I_i)$, and bending stiffness matrix $(\boldsymbol{K}_i = \mathrm{diag}(E_iI_i,\ E_iI_i,\ G_iJ_i)$, assuming rotational symmetry of the rod cross-sections. Then, deformation of the CTR is determined by the sum of internal forces and moments in each rod:

$$\boldsymbol{n}(s) = \textstyle\sum_{i=1}^{N} \boldsymbol{n}_i, \quad \boldsymbol{m}(s) = \textstyle\sum_{i=1}^{N} \boldsymbol{m}_i, \quad N = 2. \quad (2)$$

The two-rod CTR material state vector is defined as [20]

$$\boldsymbol{y}(s) = \langle \boldsymbol{p}_1 \quad \boldsymbol{q}_1 \quad \boldsymbol{n} \quad \boldsymbol{m}^b_{\mathrm{xy}} \quad m^b_{1,\mathrm{z}} \quad m^b_{2,\mathrm{z}} \quad \theta_2 \rangle, \quad (3)$$

where $\boldsymbol{m}^b_{\mathrm{xy}} \in \mathbb{R}^2$ denotes the xy-component of $\boldsymbol{m}$ expressed in the body frame of tube $i = 1$, $m^b_{i,\mathrm{z}} \in \mathbb{R}$ is the z-component of $\boldsymbol{m}_i$ expressed in the body frame of tube i, and $\theta_2 \in \mathbb{R}$ is the rotation of body frame 2 with respect to body frame 1 about the common z-axis.

Deformation of a CTR as a result of relative configurations of concentric-tubes can again be solved as a BVP [20], with the ODEs being summarized in Table I.

C. Arc-Parameterized (pre-)curvature

Cosserat rod-inspired models map the reference (unloaded) configuration of rods to a deformed (loaded) configuration. The (un)loaded rod configuration is described by a pre-curvature vector $(\boldsymbol{u}^*(s))$ and curvature vector $(\boldsymbol{u}(s))$, respectively. Characteristic for shape-lockable rods such as AGCs is that the deformed state can be assigned as a new reference configuration after shape locking, i.e. $\boldsymbol{u}^*(s) \leftarrow \boldsymbol{u}(s)$. Therefore, it is required to be able to formulate $\boldsymbol{u}(s)$ from the shape solution of the associated BVP, (1).

The (pre-)curvature vectors are obtained from continuous vector functions in the arc-centerline parameter (s), which can be computed from the continuous centerline curve $(\boldsymbol{p}(s))$. However, the shape solution only provides $\boldsymbol{p}(d\Delta s) \leftarrow \boldsymbol{Y},\ d \in \{1, 2, \dots, D\}$ at discrete points along the centerline, (1). Forming a continuous function in s from discrete points is referred to as arc-parameterization.

1) Arc-Parameterized Position: Given known positions $(\boldsymbol{p}(d\Delta s))$ at discrete centerline points, a ζ-order 3D polynomial $(\boldsymbol{p}(s) \in \mathbb{R}^3, \zeta \in \mathbb{Z}^+)$ can be fit [23]. Fitting $\boldsymbol{p}(s)$ can be achieved with linear least squares, giving the arc-parameterized centerline curve of the form

$$\begin{bmatrix} \boldsymbol{c}_\zeta \\ \vdots \\ \boldsymbol{c}_1 \end{bmatrix} = \begin{bmatrix} (1\Delta s)^\zeta \mathcal{I}_3 & \dots & (1\Delta s)\mathcal{I}_3 \\ \vdots & \ddots & \vdots \\ (D\Delta s)^\zeta \mathcal{I}_3 & \dots & (D\Delta s)\mathcal{I}_3 \end{bmatrix}^\dagger \begin{bmatrix} \boldsymbol{p}(1\Delta s) - \boldsymbol{p}(0) \\ \vdots \\ \boldsymbol{p}(D\Delta s) - \boldsymbol{p}(0) \end{bmatrix},$$

$$\boldsymbol{p}(s) = \boldsymbol{c}_\zeta s^\zeta + \dots + \boldsymbol{c}_1\, s + \boldsymbol{p}(0), \quad (6)$$

where $\boldsymbol{c}_\zeta \in \mathbb{R}^3$ and $[*]^\dagger$ represents the Moore-Penrose pseudoinverse. The centerline curve is subsequently used within Frenet-Serret formulas to define arc-parameterized orthonormal reference frames.

2) Arc-Parameterized Orientation: Frenet-Serret frames provide closed-form equations to formulate orthonormal reference frames $(\boldsymbol{R}(s) \in \mathrm{SO}(3))$ using a tangent $(\boldsymbol{t}(s))$, principal normal $(\boldsymbol{r}(s))$, and binormal $(\boldsymbol{b}(s))$ unit vector:

$$\boldsymbol{t}(s) = \tfrac{\dot{\boldsymbol{p}}}{\|\dot{\boldsymbol{p}}\|}, \quad \boldsymbol{r}(s) = \tfrac{\dot{\boldsymbol{p}}\times\ddot{\boldsymbol{p}}}{\|\dot{\boldsymbol{p}}\times\ddot{\boldsymbol{p}}\|} \times \boldsymbol{t}, \quad \boldsymbol{b}(s) = \tfrac{\dot{\boldsymbol{p}}\times\ddot{\boldsymbol{p}}}{\|\dot{\boldsymbol{p}}\times\ddot{\boldsymbol{p}}\|}. \quad (7)$$

Authorized licensed use limited to: University of Groningen. Downloaded on February 16,2024 at 12:25:47 UTC from IEEE Xplore. Restrictions apply.

TABLE I
STATIC COSSERAT ROD ORDINARY DIFFERENTIAL EQUATIONS (ODE) FOR CONCENTRIC-TUBE ROBOTS [20].

$$\dot{\boldsymbol{p}}_1(s) = \boldsymbol{R}(\boldsymbol{q}_1)\boldsymbol{v} \tag{4a}$$

$$\dot{\boldsymbol{q}}_1(s) = 0.5 \begin{bmatrix} -\mathrm{Im}(\boldsymbol{q}_1)^{\mathrm{T}} \\ \mathrm{Re}(\boldsymbol{q}_1)\mathcal{I}_3 - [\mathrm{Im}(\boldsymbol{q}_1)]_\times \end{bmatrix} \boldsymbol{R}(\boldsymbol{q}_1)\boldsymbol{u}_1 \tag{4b}$$

$$\dot{\boldsymbol{n}}(s) = -\textstyle\sum_{i=1}^{N} \boldsymbol{f}_i^b \tag{4c}$$

$$\dot{\boldsymbol{m}}_{xy}^b(s) = \{[\boldsymbol{u}_1]_\times \boldsymbol{m}^b - [\hat{\boldsymbol{z}}]_\times \boldsymbol{R}(\boldsymbol{q}_1)^{\mathrm{T}} \boldsymbol{n}\}_{\mathrm{xy}} \tag{4d}$$

$$\dot{m}_{i,z}^b(s) = -\hat{\boldsymbol{z}}^{\mathrm{T}}[\boldsymbol{u}_i]_\times \boldsymbol{m}_i^b \tag{4e}$$

$$\dot{\theta}_i(s) = u_{i,z} - u_{1,z} \tag{4f}$$

$$\boldsymbol{u}_{1,xy}(s) = (\boldsymbol{m}_{xy}^b + \textstyle\sum_{i=1}^{N} E_i I_i \boldsymbol{R}_z(\theta_i)\boldsymbol{u}_{i,xy}^*)/(\sum_{i=1}^{N} E_i I_i) \tag{5a}$$

$$u_{i,z}(s) = (m_{i,z}^b + G_i J_i u_{i,z}^*)/(G_i J_i) \tag{5b}$$

$$\boldsymbol{u}_i(s) = \boldsymbol{R}_z(\theta_i)\boldsymbol{u}_1 + \dot{\theta}_i \hat{\boldsymbol{z}} \tag{5c}$$

$$\boldsymbol{m}_i^b(s) = \boldsymbol{K}_i(\boldsymbol{u}_i - \boldsymbol{u}_i^*) \tag{5d}$$

$$\boldsymbol{m}^b(s) = \textstyle\sum_{i=1}^{N} \boldsymbol{R}_z(\theta_i)\boldsymbol{m}_i^b \tag{5e}$$

Definitions: centerline parameter (s), position ($\boldsymbol{p} \in \mathbb{R}^3$), orientation quaternion($\boldsymbol{q} \in \mathbb{H}$), internal force ($\boldsymbol{n} \in \mathbb{R}^3$), internal moment ($\boldsymbol{m} \in \mathbb{R}^3$), relative base rotation ($\theta \in \mathbb{R}$), external force ($\boldsymbol{f}_i^b \in \mathbb{R}^3$), strain vector ($\boldsymbol{v} \in \mathbb{R}^3$), curvature vector ($\boldsymbol{u}_i \in \mathbb{R}^3$), pre-curvature vector ($\boldsymbol{u}_i^* \in \mathbb{R}^3$), elastic modulus ($E_i \in \mathbb{R}$), shear modulus($G_i \in \mathbb{R}$), second moment of area ($I_i \in \mathbb{R}$), polar moment of area ($J_i \in \mathbb{R}$), and bending stiffness matrix ($\boldsymbol{K}_i \in \mathbb{R}^{3\times3}$), for i $\in \{1, \ldots, N\}$ nested rods. notations: $*_i^b$ represents a variable of rod i in the reference (body) frame of rod 1, $\hat{*}$ a unit-vector, $[*]_\times : \mathbb{R}^3 \to \mathbb{R}^{3\times3}$ a mapping to a skew symmetric matrix, and $\dot{*} := \partial * / \partial s$. explicit dependence on (s) by the variables on the right-hand side in equations (2A)–(2F) and (3A)–(3E) has been omitted for readability.

The principal normal has been denoted as $\boldsymbol{r}(s)$ instead of the more common $\boldsymbol{n}(s)$, to not confuse with the notation for internal force in Cosserat rod theory [24].

The tangent and normal vectors describe the rod bending plane, while the binormal vector represents the rotation axis. Arc-derivatives of the Frenet-Serret frame axes are given by

$$\frac{\partial \boldsymbol{t}}{\partial s} = \kappa \boldsymbol{r}, \quad \frac{\partial \boldsymbol{r}}{\partial s} = -\kappa \boldsymbol{t} + \tau \boldsymbol{b}, \quad \frac{\partial \boldsymbol{b}}{\partial s} = -\tau \boldsymbol{r}, \tag{8}$$

where $\kappa(s)$ and $\tau(s)$ represent the curvature and torsion of $\boldsymbol{p}(s)$, defined as

$$\kappa(s) = \frac{\|\dot{\boldsymbol{p}} \times \ddot{\boldsymbol{p}}\|}{\|\dot{\boldsymbol{p}}\|^3}, \quad \tau(s) = \frac{(\dot{\boldsymbol{p}} \times \ddot{\boldsymbol{p}}) \cdot \dddot{\boldsymbol{p}}}{\|\dot{\boldsymbol{p}} \times \ddot{\boldsymbol{p}}\|^2}. \tag{9}$$

Notably, $\tau(s)$ sets the minimum order of $\boldsymbol{p(s)}$ to three. Then, the arc-parameterized Frenet-Serret frame and its derivative are defined as:

$$\boldsymbol{R}(s) = \begin{bmatrix} \boldsymbol{r}, & \boldsymbol{b}, & \boldsymbol{t} \end{bmatrix}, \quad \dot{\boldsymbol{R}}(s) = \begin{bmatrix} \dot{\boldsymbol{r}}, & \dot{\boldsymbol{b}}, & \dot{\boldsymbol{t}} \end{bmatrix}, \tag{10}$$

where $\dot{\boldsymbol{r}} := \partial \boldsymbol{r} / \partial s$; similarly for $\dot{\boldsymbol{b}}$ and $\dot{\boldsymbol{t}}$. The reference frames and its arc-derivatives are required to compute the rod curvature vector.

3) Arc-Parameterized Curvature: The curvature vector ($\boldsymbol{u}(s) \in \mathbb{R}^3$) describes how the Frenet-Serret frame ($\boldsymbol{R}(s)$) changes along the centerline parameter (s). Given $\boldsymbol{R}(s)$ and $\dot{\boldsymbol{R}}(s)$, the curvature vector is computed as

$$\boldsymbol{u}(s) = \left(\boldsymbol{R}(s)^{\mathrm{T}} \dot{\boldsymbol{R}}(s)\right)^{\vee}, \tag{11}$$

where $[*]^{\vee} : \mathbb{R}^{3\times3} \to \mathbb{R}^3$ extracts the three-dimensional vector ($\boldsymbol{u}(s)$) from the skew-symmetric matrix [25]. This arc-parameterized curvature vector can be assigned to a Cosserat rod as a new pre-curvature vector ($\boldsymbol{u}^*(s) \leftarrow \boldsymbol{u}(s)$), setting the deformed shape as the updated reference configuration. We note that, when a pre-curvature ($\boldsymbol{u}^*(s)$) is assigned to a Cosserat rod, then $\boldsymbol{R}(s=0)$ should be used as a proximal boundary condition for orientation ($\boldsymbol{q}(0) \leftarrow \boldsymbol{R}(0)$).

III. METHODS

In this section, a simulation framework is presented that is used to magnetically configure the AGC shape in order to guide a needle towards a target position, shown in Fig. 2(A)–(C). The concentric arrangement of the AGC and needle is considered as a balanced-stiffness CTR.

The following nomenclature is used to interchangeably denote the Cosserat rod model and physical AGC (rod 1) in rubber (flexible) and glass (stiff) phase, needle (rod 2), and AGC-needle CTR: unloaded flexible AGC ($\mathcal{C}_{1,\mathrm{f}}^*$); loaded flexible AGC ($\mathcal{C}_{1,\mathrm{f}}$); loaded and stiffened AGC ($\mathcal{C}_{1,\mathrm{s}}$), needle ($\mathcal{C}_2$); and AGC-needle CTR ($\mathcal{C}_{12,\mathrm{s}} \leftarrow (\mathcal{C}_{1,\mathrm{s}}, \mathcal{C}_2)$).

The pre-curvatures of $\mathcal{C}_{1,\mathrm{f}}^*$ and $\mathcal{C}_2$ are considered constant ($\boldsymbol{u}_{1,\mathrm{f}}^*(s) = \boldsymbol{u}_2^*(s) = \langle 0, 0, 0 \rangle$). Further, the pre-curvature of $\mathcal{C}_{1,\mathrm{s}}$ is variable and equal to the curvature of $\mathcal{C}_{1,\mathrm{f}}$ at the point of stiffening ($\boldsymbol{u}_{1,\mathrm{s}}^* \leftarrow \boldsymbol{u}_{1,\mathrm{f}}$). Finally, $\mathcal{C}_{12,\mathrm{s}}$ depends on the pre-curvatures of $\mathcal{C}_{1,\mathrm{s}}$ and $\mathcal{C}_2$. Herein, reconfiguration of $\boldsymbol{u}_{1,\mathrm{s}}^*$ is achieved by exerting a magnetic torque ($\boldsymbol{\tau}_{\mathrm{mag}}$) on $\mathcal{C}_{1,\mathrm{f}}^*$.

First, the simulation framework is presented that is used to compute required magnetic torques on the AGC tip for shape reconfiguration. Second, a method for generating the associated magnetic field with an electromagnetic actuation system is discussed. Finally, the fabrication of the AGC and its stiffness characterization is described.

A. Simulation Framework

The simulation framework considers the AGC and needle as Cosserat rods, and their concentric configuration as a balanced-stiffness CTR. The deformation of a rod by external magnetic loading, or internal loading by relative translation of rods in a CTR, is solved as a BVP.

1) Boundary Value Problem: Herein, each BVP considers the AGC to have a constant length (l_1) and needle to have a variable length ($l_2 \in [0, l_1]$), shown in Fig. 2(D). Each rod is subjected to a distributed gravitational force ($\boldsymbol{f}_{i,\mathrm{g}}^b(s)$, expressed in the local AGC body frame.

For the proximal boundary condition, the AGC is fixed at the base ($s = 0$) with invariant position ($\boldsymbol{p}_1(0)$) and orientation ($\boldsymbol{q}_1(0)$). In addition, because the needle is straight, any axial rotation with respect to the AGC (θ_2) is considered inconsequential to the CTR shape and therefore set to zero. Internal forces and moments are unknown and grouped in a proximal optimization vector ($\boldsymbol{\xi}(0) = \langle \boldsymbol{n}(0), \boldsymbol{m}_{\mathrm{xy}}^b(0), m_{1,\mathrm{z}}^b(0), m_{2,\mathrm{z}}^b(0) \rangle$).

The intermediate boundary condition ($s = l_2$) concerns the axial internal moment ($m_{2,\mathrm{z}}^b(l_2)$) at the needle tip. Because

Authorized licensed use limited to: University of Groningen. Downloaded on February 16,2024 at 12:25:47 UTC from IEEE Xplore. Restrictions apply.

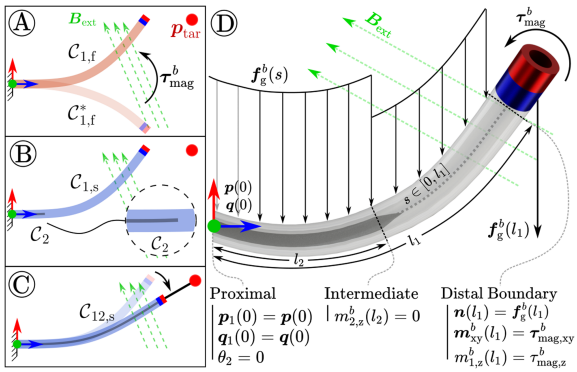

Fig. 2. Schematic representation of the simulation framework and Cosserat rod-inspired modeling of rod deflection under external loads. Ⓐ Over-deflection of an AGC in the flexible rubber phase from its undeformed ($\mathcal{C}^*_{1,\mathrm{f}}$) to deformed ($\mathcal{C}_{1,\mathrm{f}}$) state towards a target position ($\boldsymbol{p}_{\mathrm{tar}}$) by a magnetic torque ($\boldsymbol{\tau}^b_{\mathrm{mag}}$) exerted by an external field ($\boldsymbol{B}_{\mathrm{ext}}$). Ⓑ Cooling of the AGC towards the stiff glass phase for shape locking ($\mathcal{C}_{1,\mathrm{s}} \leftarrow \mathcal{C}_{1,\mathrm{f}}$). Introduction of needle ($\mathcal{C}_2$). Ⓒ Passing of needle induces deformation of $\mathcal{C}_{1,\mathrm{s}}$, representing a balanced-stiffness concentric-tube robot (CTR). The CTR ($\mathcal{C}_{12,\mathrm{s}} \leftarrow (\mathcal{C}_{1,\mathrm{s}}, \mathcal{C}_2)$) aligns with the target position. Ⓓ Boundary value problem representation for computing AGC deformation as a result of external loading or needle passing. AGC (length l_1) with centerline parameter ($s \in [0, l_1]$), base position $\boldsymbol{p}(s=0)$ and orientation $\boldsymbol{q}(0)$, distributed ($\boldsymbol{f}^b_{\mathrm{g}}(s)$) and point tip ($\boldsymbol{f}^b_{\mathrm{g}}(l_1)$) gravitational force, and magnetic torque ($\boldsymbol{\tau}^b_{\mathrm{mag}}$). Needle (length $l_2 \in [0, l_1]$) having relative base rotation (θ_2) with respect to the AGC, and tip axial moment ($m^b_{2,\mathrm{z}}$).

the needle is considered unloaded within the AGC, $m^b_{2,\mathrm{z}}(l_2)$ is assigned a zero value.

For the distal boundary condition, the AGC tip ($s = l_1$) experiences a point gravitational force ($\boldsymbol{f}^b_{\mathrm{g}}(l_1) \in \mathbb{R}^3$) and magnetic torque ($\boldsymbol{\tau}^b_{\mathrm{mag}} \in \mathbb{R}^3$) due to an external magnetic field ($\boldsymbol{B}_{\mathrm{ext}} \in \mathbb{R}^3$), providing a boundary condition for internal force ($\boldsymbol{n}(l_1)$) and moment ($\boldsymbol{m}^b_1(l_1)$), respectively.

Solving a BVP is achieved as follows. Starting from the proximal state vector ($\boldsymbol{y}(0) = \boldsymbol{y}(\boldsymbol{p}_1(0), \boldsymbol{q}(0), \theta_2, \boldsymbol{\xi})$), equation (3), the state parameters are forward integrated using the static Cosserat rod ODEs, equations (4a)-(5e), using a fourth-order Runge-Kutta method. Thereafter, the errors between the intermediate and distal boundary conditions and the associated integrated state parameters are used to update the proximal optimization vector ($\boldsymbol{\xi}(0)$) using Levenberg-Marquardt convex optimization [22].

2) AGC Shape Configuration: The simulation framework for finding the required magnetic torque ($\boldsymbol{\tau}^b_{\mathrm{mag}}$) for shape configuration of the AGC, is schematically represented in Fig. 3(A1)–(A3). The algorithm attempts to find the required $\boldsymbol{\tau}^b_{\mathrm{mag}}$ on $\mathcal{C}^*_{1,\mathrm{f}}$, such that stiffening of $\mathcal{C}_{1,\mathrm{f}}$ to $\mathcal{C}_{1,\mathrm{s}}$ and subsequent passing of $\mathcal{C}_2$, minimizes the angular targeting error (α) between $\mathcal{C}_{12,\mathrm{s}}$ and a target position ($\boldsymbol{p}_{\mathrm{tar}}$).

Within the local AGC body frame, the magnetic torque is only considered about the xy-axes as its magnet is axially-magnetized. Thus, the problem of computing the error-minimizing torque is formulated as

$$\boldsymbol{\tau}^b_{\mathrm{mag,xy}} \leftarrow \arg\min_{\boldsymbol{\tau}^b_{\mathrm{mag,xy}}} \alpha. \tag{12}$$

The process of computing $\boldsymbol{\tau}^b_{\mathrm{mag,xy}}$ involves an interative numerical optimization routine, shown in 3(B). Given a guess for $\boldsymbol{\tau}^b_{\mathrm{mag}} = \langle \boldsymbol{\tau}^b_{\mathrm{mag,xy}}, 0 \rangle$ which represents a distal boundary condition for all BVPs within an interation, the deflection of $\mathcal{C}^*_{1,\mathrm{f}}$ to $\mathcal{C}_{1,\mathrm{f}}$ is computed as a BVP, providing a discretized shape solution $\boldsymbol{Y}_{1,\mathrm{f}}$, (1).

Discrete centerline positions ($\boldsymbol{p}_{1,\mathrm{f}}(d\Delta s) \leftarrow \boldsymbol{Y}_{1,\mathrm{f}}$), are used to compute an arc-parameterized centerline curve ($\boldsymbol{p}_{1,\mathrm{f}}(s)$), Frenet-Serret frames ($\boldsymbol{R}(s)$), and curvature vector ($\boldsymbol{u}_{1,\mathrm{f}}(s)$), (6)–(11). The curvature vector is then assigned as a pre-curvature vector to $\mathcal{C}_{1,\mathrm{s}}$ ($\boldsymbol{u}^*_{1,\mathrm{s}}(s) = \boldsymbol{u}_{1,\mathrm{f}}(s)$).

Thereafter, $\mathcal{C}_{1,\mathrm{s}}$ and $\mathcal{C}_2$ are combined to form $\mathcal{C}_{12,\mathrm{s}}$, representing the CTR with a stiffened AGC and fully inserted needle ($l_2 = l_1$). The CTR shape is again solved as a BVP, providing a shape solution ($\boldsymbol{Y}_{12,\mathrm{s}}$) and associated centerline curve ($\boldsymbol{p}_{12,\mathrm{s}}(s)$). The CTR tip position and direction ($\{\boldsymbol{p}_{12}(l_1), \hat{\boldsymbol{p}}_{12}(l_1)\}$), as well as known target position ($\boldsymbol{p}_{\mathrm{tar}}$), are used to compute the targeting error,

$$\hat{\boldsymbol{p}}_{12,\mathrm{s}}(l_1) = \widehat{\boldsymbol{p}_{12,\mathrm{s}}(l_1) - \boldsymbol{p}_{12,\mathrm{s}}(l_1\text{-}\Delta s)}, \tag{13}$$

$$\hat{\boldsymbol{p}}_{\mathrm{tar},12}(l_1)) = \widehat{\boldsymbol{p}_{\mathrm{tar}} - \boldsymbol{p}_{12,\mathrm{s}}(l_1)}, \tag{14}$$

$$\alpha = \cos^{-1}\left(\hat{\boldsymbol{p}}_{12,\mathrm{s}}(l_1) \cdot \hat{\boldsymbol{p}}_{\mathrm{tar},12}(l_1)\right), \tag{15}$$

where $\hat{*}$ denotes a unit-vector. If α falls below a threshold, the solution for $\boldsymbol{\tau}^b_{\mathrm{mag}}$ is accepted. Otherwise $\boldsymbol{\tau}^b_{\mathrm{mag}}$ is updated.

In order to update $\boldsymbol{\tau}^b_{\mathrm{mag}}$, a Jacobian matrix ($\boldsymbol{J}$) is computed that relates increments in torque ($\delta\boldsymbol{\tau}^b_{\mathrm{mag,xy}}$) to changes in targeting error ($\delta\alpha$). Given the targeting angular error for some torque ($\alpha(\boldsymbol{\tau}^b_{\mathrm{mag,xy}})$), and the error for an incremented torque ($\alpha(\boldsymbol{\tau}^b_{\mathrm{mag,xy}} + d\boldsymbol{\tau}^b_{\mathrm{mag,xy}})$), the Jacobian is defined as

$$\boldsymbol{J} = \left(\frac{\alpha(\boldsymbol{\tau}^b_{\mathrm{mag,xy}} + d\boldsymbol{\tau}^b_{\mathrm{mag,xy}}) - \alpha(\boldsymbol{\tau}^b_{\mathrm{mag,xy}})}{(d\boldsymbol{\tau}^b_{\mathrm{mag,xy}})^{\mathrm{T}}}\right), \tag{16}$$

Then, the torque step is computed as

$$\Delta\boldsymbol{\tau}^b_{\mathrm{mag,xy}} = -\left(\boldsymbol{J}^{\mathrm{T}}\boldsymbol{J} + \lambda\mathcal{I}_2\right)^{-1}\boldsymbol{J}^{\mathrm{T}}\alpha, \tag{17}$$

where $\lambda \in \mathbb{R}^+$ is a damping factor.

B. Magnetic Actuation

A transformation ${}^a\boldsymbol{H}_b = ({}^a\boldsymbol{R}_b, {}^a\boldsymbol{p}_b) \in \mathrm{SE}(3)$ is defined that maps the local AGC body frame to a reference actuation frame. Then, the torque represented in the actuation frame is given by $\boldsymbol{\tau}_{\mathrm{mag}} = {}^a\boldsymbol{R}_b\boldsymbol{\tau}^b_{\mathrm{mag}}$. An external magnetic field ($\boldsymbol{B}_{\mathrm{ext}}$) exerts the desired $\boldsymbol{\tau}_{\mathrm{mag}}$ on the AGC tip magnet.

The magnetic torque ($\boldsymbol{\tau}_{\mathrm{mag}}$) and force ($\boldsymbol{f}_{\mathrm{mag}}$) exerted by $\boldsymbol{B}_{\mathrm{ext}}$ on a dipole ($\boldsymbol{\mu}_{\mathrm{mag}}$) at position ($\boldsymbol{p}_{\mathrm{mag}}$), is given by

$$\boldsymbol{\tau}_{\mathrm{mag}} = [\boldsymbol{\mu}_{\mathrm{mag}}]_\times \boldsymbol{B}_{\mathrm{ext}}(\boldsymbol{p}_{\mathrm{mag}}) \tag{18}$$

$$\boldsymbol{f}_{\mathrm{mag}} = \nabla\boldsymbol{B}_{\mathrm{ext}}(\boldsymbol{p}_{\mathrm{mag}})\boldsymbol{\mu}_{\mathrm{mag}}, \tag{19}$$

where $\nabla = (\partial/\partial x, \partial/\partial y, \partial/\partial z)$ is the gradient function, $\boldsymbol{p}_{\mathrm{mag}} = {}^a\boldsymbol{R}_b\boldsymbol{p}_{1,\mathrm{f}}(l_1) + {}^a\boldsymbol{p}_b$ is obtained from the last computed BVP shape solution, and $\boldsymbol{\mu}_{\mathrm{mag}} = {}^a\boldsymbol{R}_b\hat{\boldsymbol{p}}_{1,\mathrm{f}}(l_1)\mu_{\mathrm{mag}}$, with $\hat{\boldsymbol{p}}_{1,\mathrm{f}}(l_1)$ computed similarly to (13) and μ_{mag} the dipole moment magnitude of the AGC tip magnet.

The simulation framework discussed above assumes uniformity of the magnetic field ($i.e. \boldsymbol{f}_{\mathrm{mag}} = \langle 0, 0, 0 \rangle$) such that $\boldsymbol{\tau}_{\mathrm{mag}}$ is a unique solution for a desired AGC shape. Therefore, $\boldsymbol{B}_{\mathrm{ext}}$ can be found from (18).

Herein, $\boldsymbol{B}_{\mathrm{ext}}$ is generated by a magnetic actuation system comprising six mobile coils with actuation parameters including

Authorized licensed use limited to: University of Groningen. Downloaded on February 16,2024 at 12:25:47 UTC from IEEE Xplore. Restrictions apply.

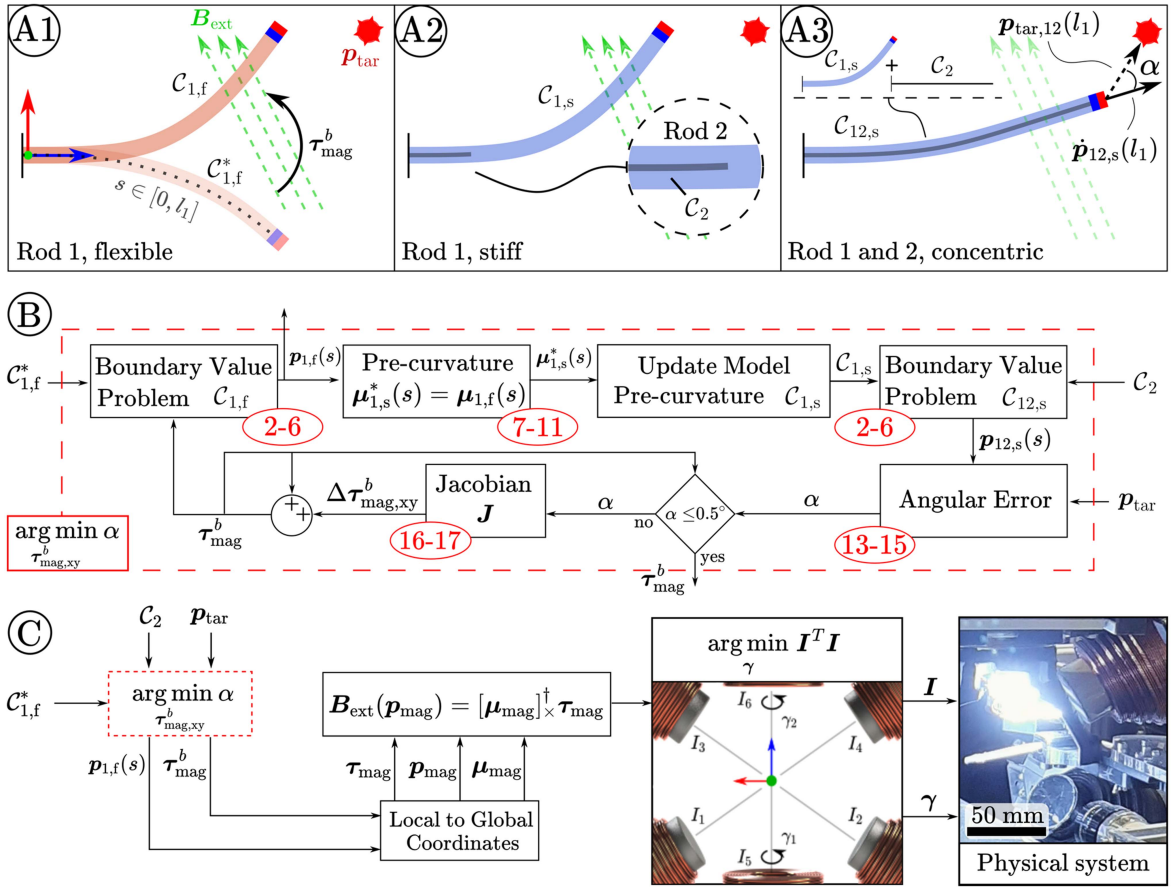

Fig. 3. Simulation framework. (A1) Unloaded rubber-phase active guiding catheter (AGC, $\mathcal{C}^*_{1,\mathrm{f}}$) with length ($l_1$) and centerline parameter (s) is deflected ($\mathcal{C}_{1,\mathrm{f}}$) by a magnetic torque ($\boldsymbol{\tau}^b_{\mathrm{mag}}$) from an external field ($\boldsymbol{B}_{\mathrm{ext}}$) towards a target position ($\boldsymbol{p}_{\mathrm{tar}}$). (A2) AGC cools down and stiffens ($\mathcal{C}_{1,\mathrm{s}}$), assuming a new pre-curvature. A needle ($\mathcal{C}_2$) is introduced. (A3) Insertion of the needle causes $\mathcal{C}_{1,\mathrm{s}}$ to deflect backward, resulting in a concentric configuration ($\mathcal{C}_{12,\mathrm{s}}$). The distal tip of $\mathcal{C}_{12,\mathrm{s}}$ has an axial direction vector ($\dot{\boldsymbol{p}}_{12,\mathrm{s}}$) and tip-target vector ($\boldsymbol{p}_{\mathrm{tar},12}$), with an angular error (α). (B) Numerical optimization algorithm minimizes α by computing the appropriate $\boldsymbol{\tau}^b_{\mathrm{mag}}$. In each iteration, $\boldsymbol{\tau}^b_{\mathrm{mag}}$ is updated, resulting in a new centerline polynomial ($\boldsymbol{p}_{1,\mathrm{f}}(s)$) for $\mathcal{C}_{1,\mathrm{f}}$. The associated curvature vector ($\boldsymbol{u}_{1,\mathrm{f}}(s)$) assigned as the pre-curvature vector ($\boldsymbol{u}^*_{1,\mathrm{s}}(s)$) for $\mathcal{C}_{1,\mathrm{s}}$. Then, concentric shape ($\mathcal{C}_{12,\mathrm{s}}$) is solved, and the distal position ($\boldsymbol{p}_{12,\mathrm{s}}(l_1)$) and axial direction vector ($\dot{\boldsymbol{p}}_{12,\mathrm{s}}(l_1)$) are obtained. These values are used to compute α, determining whether $\boldsymbol{\tau}^b_{\mathrm{mag}}$ is updated or accepted as a solution. Associated equation numbers are shown in the red elipsoids. (C) Solution for $\boldsymbol{\tau}^b_{\mathrm{mag}}$ and AGC centerline polynomial $\boldsymbol{p}_{1,\mathrm{f}}(s)$ are transformed to global reference coordinates of the actuation workspace. These values are used to compute tip-magnet position ($\boldsymbol{p}_{\mathrm{mag}}$), dipole moment ($\boldsymbol{\mu}_{\mathrm{mag}}$), and required field ($\boldsymbol{B}_{\mathrm{ext}}$). The field is generated by an electromagnetic actuation system utilizing six mobile coils [26].

angular positions ($\boldsymbol{\gamma} \in \mathbb{R}^2$) and currents ($\boldsymbol{I} \in \mathbb{R}^C$, $C = 6$), shown in Fig. 3(C) [26]. Each coil ($c \in \{1, \ldots, C\}$) contributes magnetic fields and gradients

$$\boldsymbol{B}_{\mathrm{ext},c}(\boldsymbol{\gamma}, I_c, \boldsymbol{p}_{\mathrm{mag}}) = \boldsymbol{\beta}_{\mathrm{ext},c}(\boldsymbol{\gamma}, \boldsymbol{p}_{\mathrm{mag}}) I_c, \tag{20}$$

$$\nabla \boldsymbol{B}_{\mathrm{ext},c}(\boldsymbol{\gamma}, I_c, \boldsymbol{p}_{\mathrm{mag}}) = \nabla \boldsymbol{\beta}_{\mathrm{ext},c}(\boldsymbol{\gamma}, \boldsymbol{p}_{\mathrm{mag}}) I_c, \tag{21}$$

where $\boldsymbol{\beta}_{\mathrm{ext},c} \in \mathbb{R}^3$ and $\nabla \boldsymbol{\beta}_{\mathrm{ext},c} \in \mathbb{R}^{3\times 3}$ are coil-specific unit-current field vector and gradient matrix functions, respectively [22]. Then, the torque and force on a dipole within the actuation workspace is given by

$$\begin{aligned} \boldsymbol{\tau}_{\mathrm{mag}} &= \sum_{c=1}^{C} \underbrace{[\boldsymbol{\mu}_{\mathrm{mag}}]_\times \boldsymbol{\beta}_{\mathrm{ext},c}(\boldsymbol{\gamma}, \boldsymbol{p}_{\mathrm{mag}})}_{\boldsymbol{\tau}_{\mathrm{mag},c}} I_c \\ &= \begin{bmatrix} \boldsymbol{\tau}_{\mathrm{mag},1} & \ldots & \boldsymbol{\tau}_{\mathrm{mag},C} \end{bmatrix} \boldsymbol{I} = \boldsymbol{T}_{\mathrm{mag}} \boldsymbol{I}, \end{aligned} \tag{22}$$

$$\begin{aligned} \boldsymbol{f}_{\mathrm{mag}} &= \sum_{c=1}^{C} \underbrace{\nabla \boldsymbol{\beta}_{\mathrm{ext},c}(\boldsymbol{\gamma}, \boldsymbol{p}_{\mathrm{mag}}) \boldsymbol{\mu}_{\mathrm{mag}}}_{\boldsymbol{f}_{\mathrm{mag},c}} I_c \\ &= \begin{bmatrix} \boldsymbol{f}_{\mathrm{mag},1} & \ldots & \boldsymbol{f}_{\mathrm{mag},C} \end{bmatrix} \boldsymbol{I} = \boldsymbol{F}_{\mathrm{mag}} \boldsymbol{I}. \end{aligned} \tag{23}$$

Because $\boldsymbol{\tau}_{\mathrm{mag}}$ and $\boldsymbol{f}_{\mathrm{mag}}$ are nonlinear in $\boldsymbol{\gamma}$, computing the coil current-minimizing positions is formulated as a numerical optimization problem

$$\arg\min_{\boldsymbol{\gamma}} (\boldsymbol{I}^{\mathrm{T}} \boldsymbol{I}), \quad \text{s.t. } |I_c| \leq 8 \text{ A}, \forall I_c \in \boldsymbol{I}, \tag{24}$$

where for each $\boldsymbol{\gamma}$, $\boldsymbol{I}$ is found from linear least squares

$$\boldsymbol{I} = \begin{bmatrix} \boldsymbol{T}_{\mathrm{mag}} \\ \boldsymbol{F}_{\mathrm{mag}} \end{bmatrix}^{\dagger} \begin{bmatrix} \boldsymbol{\tau}_{\mathrm{mag}} \\ \boldsymbol{f}_{\mathrm{mag}} \end{bmatrix}. \tag{25}$$

Authorized licensed use limited to: University of Groningen. Downloaded on February 16,2024 at 12:25:47 UTC from IEEE Xplore. Restrictions apply.

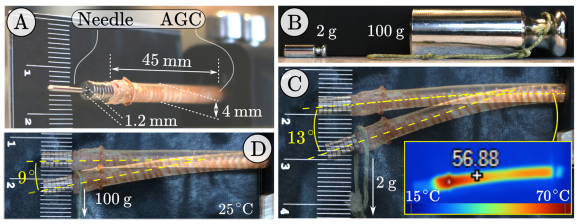

Fig. 4. Stiffness characterization of the active guiding catheter (AGC). Ⓐ Setup with a horizontally suspended AGC. Ⓑ Weights that are hung on the AGC tip to induce deflection. Ⓒ AGC in the glass phase at 25 °C room temperature with a deflection angle of $\phi = 9°$ due to a 100 g weight. Ⓓ AGC in the rubber phase at an elevated temperature approaching 60 °C with a deflection angle of $\phi = 13°$ due to a 2 g weight.

Finally, the computed solution of $\{\boldsymbol{I}, \boldsymbol{\gamma}\}$ is passed on to the physical magnetic actuation system, shown in Fig. 3(C), resulting in actuation of the AGC.

C. Fabrication and Stiffness Characterization

The AGC (ID: 1.2 mm, OD: 4 mm, L: 45 mm) consists of a PTFE tube (ID: 1.2 mm, OD: 1.4 mm, L: 45 mm), copper heating coil (0.2 mm wire diameter), and shape memory polymer (MP3510, SMPTechnologies, Japan) with a glass transition temperature of 35 °C, glass phase at ≤20 °C, and rubber phase at ≥60 °C [9]. Fabrication of the AGC was performed within a cylindrical silicone mold (SORTA-Clear 40, Smooth-On Inc., USA). Firstly, copper wire is wound around the tube, seven axially-magnetized ring magnets (N48, ID: 1.5 mm, OD: 4 mm, L: 1 mm, Neomagnete, Germany) slid over the end, and the tube is placed centrally within the mold. Secondly, the shape memory polymer is injected into the mold from a dual cartridge (50 ml 1:1 Dual Cartridge B-System, Adhesive Dispensing Ltd., U.K.) with a static mixer nozzle (MBH04-12D, Adhesive Dispensing Ltd., U.K.). Thirdly, the AGC is vulcanized at 70 °C for 2 h and removed from the mold. In addition to the AGC, the needle is a straight stainless-steel cylinder (OD: 1 mm, L: 200 mm).

1) Stiffness Characterization: The elastic moduli of the AGC in both rubber $(E_{1,\mathrm{f}})$ and glass phase $(E_{1,\mathrm{s}})$ at heated (60 °C) and room (25 °C) temperature, respectively, are required by the previously described Cosserat rod models in order to determine the curvatures of $\mathcal{C}_{1,\mathrm{f}}$ and $\mathcal{C}_{1,\mathrm{s}}$, after actuation or passing of $\mathcal{C}_2$, respectively, (5a). By considering the AGC as a tip-loaded cantilever beam, the elastic moduli are measured experimentally, Fig. 4(A)–(D), from the flexural modulus of elasticity [27]

$$E = mgl^2/2I\phi, \tag{26}$$

where m is the load mass, $g = 9.81\ \mathrm{m/s^2}$, $I = \pi(r_\mathrm{o}^4 - r_\mathrm{i}^4)/4$ the second moment of area of the AGC where r_o and r_i are the outer and inner radius, and ϕ the deflection angle. Based on the measurements, $E_{1,\mathrm{f}} \approx 7$ MPa and $E_{1,\mathrm{s}} \approx 0.5$ GPa, which is consistent with literature for the mentioned temperatures [8], [9]. Additionally, the needle is assigned the elastic modulus of stainless steel $(E_2 = 193$ GPa).

IV. Results

During experiments, the aim is for the simulation framework to inform magnetically-assisted AGC reconfiguration such that a needle is guided towards different targets.

Fig. 5 presents the experimental setup, including the horizontally-suspended unactuated AGC ($\mathcal{C}^*_{1,\mathrm{f}}$, length $l_1 = 45$ mm) and three targets (5 mm diameter) within the workspace of the magnetic actuation system. The tip of $\mathcal{C}^*_{1,\mathrm{f}}$ is located at $\langle -5, 0, 0\rangle$ mm, target 1 at $\langle 50, -2, 27\rangle$ mm, target 2 at $\langle 46, -32, 7\rangle$ mm, and target 3 at $\langle 34, 35, -30\rangle$ mm, with respect to the center of the actuation workspace.

Each target corresponds to a separate experiment conducted at 25 °C room temperature, shown in Fig. 5(T1)–(T3). First, the simulation framework computes $\boldsymbol{\tau}_\mathrm{mag}$ and associated magnetic field. Then, the actuation system is adjusted to the specified configuration and the AGC heated above 60 °C with a current of 2 A for 60 sec, resulting in the deflection of $\mathcal{C}^*_{1,\mathrm{f}}$ to $\mathcal{C}_{1,\mathrm{f}}$. Thereafter, $\mathcal{C}_{1,\mathrm{f}}$ is passively cooled for 120 sec to room temperature, causing the AGC to assume a fixed shape $(\mathcal{C}_{1,\mathrm{s}})$. Finally, $\mathcal{C}_2$ is inserted through $\mathcal{C}_{1,\mathrm{s}}$.

The volumes of $\mathcal{C}_{1,\mathrm{s}}$ and $\mathcal{C}_{12,\mathrm{s}}$ are segmented into voxels using stereo vision, as depicted in Fig. 6(A1)–(A2). An iterative reconstruction algorithm is then employed to obtain discrete centerline points from the voxels. These points are used to fit a 3D centerline polynomial, equation (6) [23].

Fig. 6(B1) shows the centerline polynomials of $\mathcal{C}_{1,\mathrm{s}}$ obtained from the simulation framework $(\boldsymbol{p}_{1,\mathrm{s}}(s))$ and voxel-based reconstruction $(\bar{\boldsymbol{p}}_{1,\mathrm{s}}(s))$. Fig. 6(B2) presents the angular difference between the axial directions of the centerline curves $(\angle\boldsymbol{p}_{1,\mathrm{s}}, \bar{\boldsymbol{p}}_{1,\mathrm{s}})$ and between the axial directions of the centerline curves and the suspending x-axis of the AGC $(\hat{\boldsymbol{x}})$. Similarly, figure 6(C1), centerline polynomials of $\mathcal{C}_{12,\mathrm{s}}$ are obtained from the simulation framework $(\boldsymbol{p}_{12,\mathrm{s}}(s))$ and voxel-based reconstruction $(\bar{\boldsymbol{p}}_{12,\mathrm{s}}(s))$, along with tangent lines aligned with their tip directions, i.e. tangent to $\boldsymbol{p}_{12,\mathrm{s}}(l_1)$ and $\bar{\boldsymbol{p}}_{12,\mathrm{s}}(l_1)$. Fig. 6(C2) indicates the angular difference between the axial directions of the centerline curves $(\angle\boldsymbol{p}_{12,\mathrm{s}}, \bar{\boldsymbol{p}}_{12,\mathrm{s}})$ and the axial directions of the centerline curves and the suspending x-axis of the AGC.

The simulated backward deflection, that is $\angle(\boldsymbol{p}_{1,\mathrm{s}}(l_1), \hat{\boldsymbol{x}})$ to $\angle(\boldsymbol{p}_{12,\mathrm{s}}(l_1), \hat{\boldsymbol{x}})$, for target 1 was 30° (48° to 18°), for target 2 it was 35° (58° to 24°), and for target 3 it was 49° (83° to 34°). Comparatively, the measured backward deflection, that is $\angle(\bar{\boldsymbol{p}}_{1,\mathrm{s}}(l_1), \hat{\boldsymbol{x}})$ to $(\angle\bar{\boldsymbol{p}}_{12,\mathrm{s}}(l_1), \hat{\boldsymbol{x}})$, for target 1 was 34° (50° to 16°), for target 2 it was 25° (47° to 22°), and for target 3 it was 39° (69° to 30°). The shortest distances between the target and needle (represented by the tangent lines to $\bar{\boldsymbol{p}}_{12,\mathrm{s}}(l_1)$) are 2.3 mm, 7.1 mm, and 7.7 mm.

Therefore, the difference between $\angle(\boldsymbol{p}_{1,\mathrm{s}}(l_1), \hat{\boldsymbol{x}})$ and $\angle(\bar{\boldsymbol{p}}_{1,\mathrm{s}}(l_1), \hat{\boldsymbol{x}})$ of the AGC for target 1 was 2° (48° and 50°), for target 2 it was 11° (58° and 47°), and for target 3 it was 14° (83° and 69°). In addition, the difference between $\angle(\boldsymbol{p}_{12,\mathrm{s}}(l_1), \hat{\boldsymbol{x}})$ and $\angle(\bar{\boldsymbol{p}}_{12,\mathrm{s}}(l_1), \hat{\boldsymbol{x}})$ of the CTR for target 1 was 2° (18° and 16°), for target 2 it was 2° (24° and 22°), and for target 3 it was 4° (34° and 30°).

Video recordings of the experiments are provided in the supplementary material. Additionally, the MATLAB implementation of the simulation framework is available online at https://github.com/MichielRichter/Active_Guiding_Catheters.

V. Discussion

The results demonstrate the simulation framework's ability to predict the backward deflection of $\mathcal{C}_{1,\mathrm{s}}$ to $\mathcal{C}_{12,\mathrm{s}}$ and provide information on the required magnetic torque for achieving $\mathcal{C}_{1,\mathrm{s}}$ from $\mathcal{C}^*_{1,\mathrm{f}}$. Needle targeting errors are associated with model inaccuracies regarding, e.g., elastic modulus, moment of area, magnetic field and gradient maps. Additionally, the magnetic torque was calculated for $\mathcal{C}^*_{1,\mathrm{f}}$ but the field generated for $\mathcal{C}_{1,\mathrm{f}}$.

Authorized licensed use limited to: University of Groningen. Downloaded on February 16,2024 at 12:25:47 UTC from IEEE Xplore. Restrictions apply.

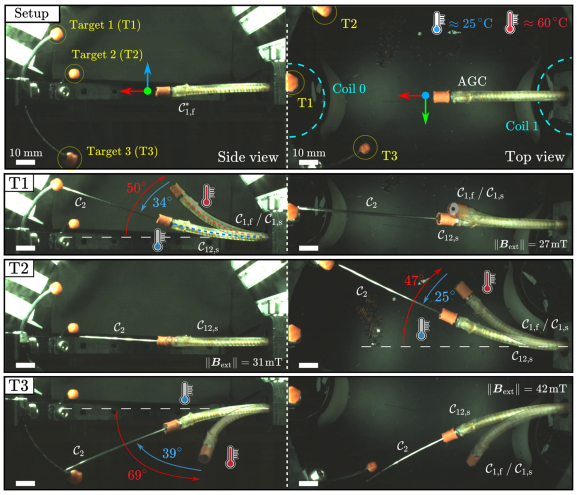

Fig. 5. Experimental results. The setup shows the horizontally suspended active guiding catheter (AGC) in its undeformed state ($\mathcal{C}^*_{1,\mathrm{f}}$), targets 1-3 (T1-T3), and two coils of the magnetic actuation system [26]. Each experiment is performed as follows. First, the AGC is heated (flexible) and magnetically deflected ($\mathcal{C}_{1,\mathrm{f}}$). Second, the AGC is passively cooled (stiffened) during 120 sec, locking its shape ($\mathcal{C}_{1,\mathrm{s}}$). Third, a needle ($\mathcal{C}_2$) is passed through the AGC, giving a concentric configuration ($\mathcal{C}_{12,\mathrm{s}}$) in elastic equilibrium and aligned with a target. *Scale bar: 10 mm.*.

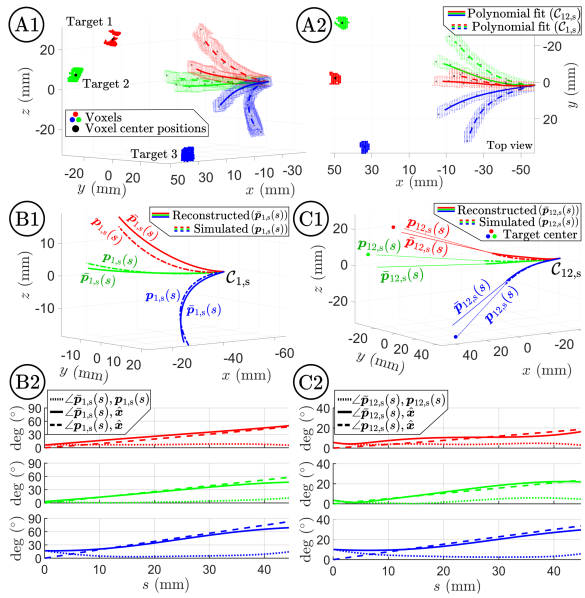

Fig. 6. Results analysis. (A1) - (A2) Segmented voxels of targets, deflected AGC ($\mathcal{C}_{1,\mathrm{s}}$), and AGC-needle ($\mathcal{C}_{12,\mathrm{s}}$) with reconstructed centerline curves, (6). (B1) Polynomial centerline curves of $\mathcal{C}_{1,\mathrm{s}}$: desired simulated curve ($\boldsymbol{p}_{1,\mathrm{s}}(s)$) and reconstructed curve ($\bar{\boldsymbol{p}}_{1,\mathrm{s}}(s)$). The curves vary with the centerline parameter ($s \in [0, l_1]$, $l_1 = 45$ mm the AGC length). (B2) For $\mathcal{C}_{1,\mathrm{s}}$, the angular deflection of the centerline curves with respect to the suspending x-axis of the AGC, and angular error between the centerline curves, along s. (C1) Centerline curves of $\mathcal{C}_{12,\mathrm{s}}$ with tangent lines to $\boldsymbol{p}_{12,\mathrm{s}}(l_1)$ and $\bar{\boldsymbol{p}}_{12,\mathrm{s}}(l_1)$. (C2) For $\mathcal{C}_{12,\mathrm{s}}$, the angular deflection of the centerline curves with respect to the suspending x-axis of the AGC, and angular error between the centerline curves, along s.

Because the torque on a dipole changes with its rotation in a field, the field should ideally move to match the AGC deflection. For moving fields the robustness of the actuation should be considered [13].

Closed-loop control can compensate for model inaccuracies [22]. However, the simulation framework's convergence time for computing the required magnetic torque reaches several minutes, which is infeasible for closed-loop control. Potential solutions for achieving future closed-loop control of balanced-stiffness AGCs and needles are discussed below.

Firstly, computation time can be reduced by making informed predictions on the required deflection of $\mathcal{C}_{1,\mathrm{s}}$ to reach a desired deflection of $\mathcal{C}_{12,\mathrm{s}}$. We observe that the measured (and simulated) backward deflection angles for each target correlates to the bending stiffness (EI) ratio of the rods. In this work, the EI-ratio ($E_2I_2/E_{1,\mathrm{s}}I_1$) between the needle and AGC is 1.57. Comparatively, the ratio of the measured deflection of $\mathcal{C}_{1,\mathrm{s}}$ ($50°, 47°, 69°$) to the backward deflection ($34°, 25°, 39°$) was 1.47, 1.88, and 1.77, respectively for each target. Therefore, a prediction of required $\mathcal{C}_{1,\mathrm{s}}$ deflection could be made based on the EI-ratio with a straight $\mathcal{C}_2$ as

$$\angle\mathcal{C}_{12,\mathrm{s}}, \mathcal{C}^*_{1,\mathrm{f}} \approx \angle\mathcal{C}_{1,\mathrm{s}}, \mathcal{C}^*_{1,\mathrm{f}} - \frac{\angle\mathcal{C}_{1,\mathrm{s}}, \mathcal{C}^*_{1,\mathrm{f}}}{1 + (E_{1,\mathrm{s}}I_1/(E_2, I_2))}. \quad (27)$$

Secondly, we observed that $\mathcal{C}_{12,\mathrm{s}}$ can be further steered over small angles ($\approx 1°$) by a field of 35 mT (supplementary video). The bending susceptibility of the CTR to the external field appears greater towards the reference configuration of the rod with the highest bending stiffness.

Thirdly, retracting the needle from $\mathcal{C}_{12,\mathrm{s}}$ allows for a new AGC stiffness transition and reconfiguration. Although the active heating and passive cooling method used in this study takes a few minutes, is impractical, and allows the AGC to slightly deviate from the initially-deflected shape during cooling (supplementary video), previous studies have shown that actively heated and cooled AGCs can achieve stiffness transition in less than 10 sec [16]. Active heating and cooling enables stiffness control. The temperature of $\mathcal{C}_{1,\mathrm{s}}$ can be regulated in the glass-transition region, whereby the backward deflection of $\mathcal{C}_{12,\mathrm{s}}$ by $\mathcal{C}_2$ becomes controllable.

Fourthly, alternative modeling approaches, such as constant-curvature models [28], [29], can improve computation time at the expense of accuracy. Additionally, the torque-optimization step can be replaced with human-in-the-loop control of the magnetic field. This approach involves imaging-based reconstruction of the AGC and predicting needle-induced deformation. In this case, one BVP is required, as opposed to solving six BVPs per iteration step as shown in Fig. 3(B). Three-dimensional reconstruction of the AGC can be achieved using various medical imaging modalities [30], such as a rotating C-arm fluoroscopy system [31], [32]. Finally, when a target is surrounded by a solid medium, it is possible to use steerable needles [33], [34].

Regarding applicability of the presented work, the outer diameter of the AGC (4 mm) is relatively large compared to metallic needle-guiding endovascular catheters [3], but chosen based on the commercial availability of the ring-shaped permanent magnets. However, the results may be generalized to combinations of needles and AGCs with similar EI-ratio. For example, an EI-ratio similar to the one in this study (1.57) can be achieved with a combination of a 22-gauge (0.7 mm) superelastic nitinol needle ($E = 50$ GPa) and an AGC with equal inner diameter, 1.7 mm outer diameter, and elastic modulus of 1 GPa (herein the AGC elastic modulus (0.5 GPA) is lower than commonly reported values [8], [9]). Such dimensions are suitable for endovascular applications such as transjugular liver biopsy [3]. However, a smaller EI-ratio is preferable as the configuration

Authorized licensed use limited to: University of Groningen. Downloaded on February 16,2024 at 12:25:47 UTC from IEEE Xplore. Restrictions apply.

of $\mathcal{C}_{12,\mathrm{s}}$ will be dominated by $\mathcal{C}_{1,\mathrm{s}}$ rather than $\mathcal{C}_2$, which facilitates larger possible deflection angles [11].

A reduction in EI-ratio may be achieved by using more flexible needles, but which may limit propagation through tissue as needle buckling becomes of concern [10].. Alternatively, the elastic modulus of the AGC can be increased. An AGC with an $E_{1,\mathrm{s}}$ of 4.1 GPa has been reported with the addition of metallic filler particles, which inherently results in an increase in $E_{1,\mathrm{f}}$ [8]. Because $E_{1,\mathrm{f}}$ affects the required magnetic field to deflect $\mathcal{C}^*_{1,\mathrm{f}}$ to $\mathcal{C}_{1,\mathrm{f}/}\mathcal{C}_{1,\mathrm{s}}$ and $E_{1,\mathrm{s}}$ affects the induced deflection by $\mathcal{C}_2$, the primary limiting factor for the application of AGCs in needle guidance is the glass stiffness.

Finally, the shape memory polymer that was used to make the AGC has a rubber-phase temperature of 60 °C [9]. However, the permitted surface temperature for endovascular applications is limited to 41 °C [16]. Therefore, the outer surface of the AGC should be insulated or be made of a shape memory polymer with a lower transition temperature.

VI. Conclusion

Shape memory polymer-based AGCs and straight metallic needles behave as balanced-stiffness CTRs. Magnetic reconfiguration of AGCs enables compensating for needle elasticity. Cosserat rod models can predict the required AGC shape, such that needle-induced backward deflection aligns the CTR with a target position. Increasing bending stiffness of the AGC compared to the needle will reduce the magnitude of needle-induced backward deflection, potentially reducing computational cost of the model.

The convergence time of the simulation framework is infeasible for closed-loop control. Human-in-the-loop control instead of the torque-optimization may reduce the number of required BVPs to solve. Also, informed predictions on the required AGC shape can be made based on the bending stiffness ratio between the AGC and needle. Further, active heating and cooling enables stiffness control of the AGC, which can be used in combination with the needle elasticity to induce relaxation and further deflection of the CTR.

Future work can address closed-loop control and miniaturization of the AGC to clinically-relevant dimensions.

References

[1] Y. Fu, H. Liu, W. Huang, S. Wang, and Z. Liang, "Steerable catheters in minimally invasive vascular surgery," *Int. J. Med. Robot. Comput. Assist. Surg.*, vol. 5, no. 4, pp. 381–391, 2009.

[2] V. Ojha and S. N. Raju, "Catheters in vascular interventional radiology: An illustrated review," *Diagn. Interventional Radiol.*, vol. 29, no. 1, pp. 138–145, 2023.

[3] A. Dohan, Y. Guerrache, M. Boudiaf, J.-P. Gavini, R. Kaci, and P. Soyer, "Transjugular liver biopsy: Indications, technique and results," *Diagn. Interventional Imag.*, vol. 95, no. 1, pp. 11–15, 2014.

[4] P. J. Swaney et al., "Toward transoral peripheral lung access: Combining continuum robots and steerable needles," *J. Med. Robot. Res.*, vol. 2, no. 1, 2017, Art. no. 1750001.

[5] H. B. Gilbert, J. Neimat, and R. J. Webster, "Concentric tube robots as steerable needles: Achieving follow-the-leader deployment," *IEEE Trans. Robot.*, vol. 31, no. 2, pp. 246–258, Apr. 2015.

[6] C. Bergeles, A. H. Gosline, N. V. Vasilyev, P. J. Codd, P. J. del Pedro, and P. E. Dupont, "Concentric tube robot design and optimization based on task and anatomical constraints," *IEEE Trans. Robot.*, vol. 31, no. 1, pp. 67–84, Feb. 2015.

[7] C. Chautems, A. Tonazzini, Q. Boehler, S. H. Jeong, D. Floreano, and B. J. Nelson, "Magnetic continuum device with variable stiffness for minimally invasive surgery," *Adv. Intell. Syst.*, vol. 2, no. 6, 2020, Art. no. 1900086.

[8] M. Mattmann et al., "Thermoset shape memory polymer variable stiffness 4D robotic catheters," *Adv. Sci.*, vol. 9, no. 1, 2022, Art. no. 2103277.

[9] T. L. Thomas, J. Bos, J. J. Huaroto, V. Kalpathy Venkiteswaran, and S. Misra, "A magnetically actuated variable stiffness manipulator based on deployable shape memory polymer springs," *Adv. Intell. Syst.*, vol. 16, 2023, Art. no. 2200465.

[10] N. J. Van De Berg,, D. J. Berg, V. Gerwen, J. Dankelman, and J. J. Van Den Dobbelsteen, "Design choices in needle steering—A review," *IEEE/ASME Trans. Mechatron.*, vol. 20, no. 5, pp. 2172–2183, Oct. 2015.

[11] P. E. Dupont, J. Lock, B. Itkowitz, and E. Butler, "Design and control of concentric-tube robots," *IEEE Trans. Robot.*, vol. 26, no. 2, pp. 209–225, Apr. 2010.

[12] D. C. Rucker, B. A. Jones, and R. J. Webster III, "A geometrically exact model for externally loaded concentric-tube continuum robots," *IEEE Trans. Robot.*, vol. 26, no. 5, pp. 769–780, Oct. 2010.

[13] J. Edelmann, A. J. Petruska, and B. J. Nelson, "Magnetic control of continuum devices," *Int. J. Robot. Res.*, vol. 36, no. 1, pp. 68–85, 2017.

[14] H. Gu et al., "Magnetic cilia carpets with programmable metachronal waves," *Nature Commun.*, vol. 11, no. 1, pp. 1–10, 2020.

[15] J. Till, V. Aloi, and C. Rucker, "Real-time dynamics of soft and continuum robots based on cosserat rod models," *Int. J. Robot. Res.*, vol. 38, no. 6, pp. 723–746, 2019.

[16] M. Mattmann, Q. Boehler, X.-Z. Chen, S. Pané, and B. J. Nelson, "Shape memory polymer variable stiffness magnetic catheters with hybrid stiffness control," in *Proc. IEEE/RSJ Int. Conf. Intell. Robots Syst.*, 2022, pp. 9589–9595.

[17] J. Lussi et al., "A submillimeter continuous variable stiffness catheter for compliance control," *Adv. Sci.*, vol. 8, no. 18, 2021, Art. no. 2101290.

[18] J. J. Abbott, E. Diller, and A. J. Petruska, "Magnetic methods in robotics," *Annu. Rev. Control Robot. Auton. Syst.*, vol. 3, pp. 57–90, 2020.

[19] S. S. Antman, "Problems in nonlinear elasticity," in *Nonlinear Problems Elasticity*. New York, NY, USA: Springer, 2005, pp. 513–584.

[20] J. Till, V. Aloi, K. E. Riojas, P. L. Anderson, R. J. Webster III, and C. Rucker, "A dynamic model for concentric tube robots," *IEEE Trans. Robot.*, vol. 36, no. 6, pp. 1704–1718, Dec. 2020.

[21] D. C. Rucker and R. J. Webster III, "Statics and dynamics of continuum robots with general tendon routing and external loading," *IEEE Trans. Robot.*, vol. 27, no. 6, pp. 1033–1044, Dec. 2011.

[22] M. Richter, V. K. Venkiteswaran, and S. Misra, "Multi-point orientation control of discretely-magnetized continuum manipulators," *IEEE Robot. Automat. Lett.*, vol. 6, no. 2, pp. 3607–3614, Apr. 2021.

[23] J. Sikorski, A. Denasi, G. Bucchi, S. Scheggi, and S. Misra, "Vision-based 3-D control of magnetically actuated catheter using bigmag–An array of mobile electromagnetic coils," *IEEE/ASME Trans. Mechatron.*, vol. 24, no. 2, pp. 505–516, Apr. 2019.

[24] R. T. Farouki, "Rational rotation-minimizing frames–recent advances and open problems," *Appl. Math. Comput.*, vol. 272, pp. 80–91, 2016.

[25] R. M. Murray, Z. Li, and S. S. Sastry, *A Mathematical Introduction to Robotic Manipulation*. Boca Raton, FL, USA: CRC, 2017.

[26] J. Sikorski, I. Dawson, A. Denasi, E. E. G. Hekman, and S. Misra, "Introducing BigMag–A novel system for 3D magnetic actuation of flexible surgical manipulators," in *Proc. IEEE Int. Conf. Robot. Automat.*, 2017, pp. 3594–3599.

[27] J. M. Gere and B. J. Goodno, *Mechanics of Materials*, 8th ed. Boston, MA, USA: Cengage Learning, 2013.

[28] R. J. Webster III and B. A. Jones, "Design and kinematic modeling of constant curvature continuum robots: A review," *Int. J. Robot. Res.*, vol. 29, no. 13, pp. 1661–1683, 2010.

[29] G. Pittiglio et al., "Closed loop static control of multi-magnet soft continuum robots," *IEEE Robot. Automat. Lett.*, vol. 8, no. 7, pp. 3980–3987, Jul. 2023.

[30] A. Ramadani, M. Bui, T. Wendler, H. Schunkert, P. Ewert, and N. Navab, "A survey of catheter tracking concepts and methodologies," *Med. Image Anal.*, vol. 22, 2022, Art. no. 102584.

[31] A. Hong, A. J. Petruska, and B. J. Nelson, "Tracking a magnetically guided catheter with a single rotating C-Arm," in *Proc. IEEE Int. Conf. Robot. Automat.*, 2015, pp. 618–623.

[32] M. Ourak et al., "Fusion of biplane fluoroscopy with fiber Bragg grating for 3D catheter shape reconstruction," *IEEE Robot. Automat. Lett.*, vol. 6, no. 4, pp. 6505–6512, Oct. 2021.

[33] P. J. Swaney, J. Burgner, H. B. Gilbert, and R. J. Webster, "A flexure-based steerable needle: High curvature with reduced tissue damage," *IEEE Trans. Biomed. Eng.*, vol. 60, no. 4, pp. 906–909, Apr. 2013.

[34] A. Hong, A. J. Petruska, A. Zemmar, and B. J. Nelson, "Magnetic control of a flexible needle in neurosurgery," *IEEE Trans. Biomed. Eng.*, vol. 68, no. 2, pp. 616–627, Feb. 2021.

Authorized licensed use limited to: University of Groningen. Downloaded on February 16,2024 at 12:25:47 UTC from IEEE Xplore. Restrictions apply.